2011

Photoelectron-photofragment coincidence spectroscopy in a cryogenically cooled linear electrostatic ion beam trap

Christopher J. Johnson
University of California - San Diego

Ben B. Shen
University of California - San Diego

Berwyck L. J Poad
University of Wollongong, bpoad@uow.edu.au

Robert E. Continetti
University of California - San Diego

Publication Details

Johnson, C. J., Shen, B. B., Poad, B. L. J. & Continetti, R. E. (2011). Photoelectron-photofragment coincidence spectroscopy in a cryogenically cooled linear electrostatic ion beam trap. Review of Scientific Instruments, 82 (10), 105105-1-105105-9.

Photoelectron-photofragment coincidence spectroscopy in a cryogenically cooled linear electrostatic ion beam trap

Abstract

A cryogenically cooled linear electrostatic ion beam trap for use in photoelectron-photofragment coincidence (PPC) spectroscopy is described. Using this instrument, anions created in cold, low-dutycycle sources can be stored for many seconds in a ~20 K environment to cool radiatively, removing energetic uncertainties due to vibrationally excited precursor anions. This apparatus maintains a well-collimated beam necessary for high-resolution fragment imaging and the high experimental duty cycle needed for coincidence experiments. Ion oscillation is bunched and phase-locked to a modelocked laser, ensuring temporal overlap between ion bunches and laser pulses and that ions are intersected by the laser only when travelling in one direction. An electron detector is housed in the field-free center of the trap, allowing PPC experiments to be carried out on ions while they are stored and permitting efficient detection of 3-dimensional electron and neutral recoil trajectories. The effects of trapping parameters on the center-of-mass trajectories in the laser-ion interaction region are explored to optimize neutral particle resolution, and the impact of bunching on ion oscillation is established. Finally, an initial demonstration of radiative cooling is presented.

Keywords

beam, ion, electrostatic, linear, trap, cooled, photoelectron, cryogenically, spectroscopy, coincidence, photofragment, GeoQUEST

Publication Details

Johnson, C. J., Shen, B. B., Poad, B. L. J. & Continetti, R. E. (2011). Photoelectron-photofragment coincidence spectroscopy in a cryogenically cooled linear electrostatic ion beam trap. Review of Scientific Instruments, 82 (10), 105105-1-105105-9.

AIP | Review of Scientific Instruments

Photoelectron-photofragment coincidence spectroscopy in a cryogenically cooled linear electrostatic ion beam trap

Christopher J. Johnson, Ben B. Shen, Berwyck L. J. Poad, and Robert E. Continetti

Citation: Rev. Sci. Instrum. 82, 105105 (2011); doi: 10.1063/1.3641875
View online: http://dx.doi.org/10.1063/1.3641875
View Table of Contents: http://rsi.aip.org/resource/1/RSINAK/v82/i10
Published by the American Institute of Physics.

Photoelectron-photofragment coincidence spectroscopy in a cryogenically cooled linear electrostatic ion beam trap

Christopher J. Johnson,[1] Ben B. Shen,[2] Berwyck L. J. Poad,[2] and Robert E. Continetti[2]
[1]*Department of Physics, University of California, San Diego, La Jolla, California 92093-0340, USA*
[2]*Department of Chemistry and Biochemistry, University of California, San Diego, La Jolla, California 92093-0340, USA*

(Received 19 July 2011; accepted 31 August 2011; published online 10 October 2011)

A cryogenically cooled linear electrostatic ion beam trap for use in photoelectron-photofragment coincidence (PPC) spectroscopy is described. Using this instrument, anions created in cold, low-duty-cycle sources can be stored for many seconds in a ~20 K environment to cool radiatively, removing energetic uncertainties due to vibrationally excited precursor anions. This apparatus maintains a well-collimated beam necessary for high-resolution fragment imaging and the high experimental duty cycle needed for coincidence experiments. Ion oscillation is bunched and phase-locked to a modelocked laser, ensuring temporal overlap between ion bunches and laser pulses and that ions are intersected by the laser only when travelling in one direction. An electron detector is housed in the field-free center of the trap, allowing PPC experiments to be carried out on ions while they are stored and permitting efficient detection of 3-dimensional electron and neutral recoil trajectories. The effects of trapping parameters on the center-of-mass trajectories in the laser-ion interaction region are explored to optimize neutral particle resolution, and the impact of bunching on ion oscillation is established. Finally, an initial demonstration of radiative cooling is presented. © *2011 American Institute of Physics*. [doi:10.1063/1.3641875]

I. INTRODUCTION

Since its introduction in the late 1990s,[1,2] the electrostatic ion beam trap (EIBT) has found a variety of uses in ion spectroscopy,[3–5] dissociation dynamics,[6,7] and mass spectrometry.[8–10] This type of device, which allows the storage of a fast (keV) beam of ions for seconds or longer, is a relatively simple and compact alternative to magnetic or electrostatic ion storage rings.[11] Several favorable properties, such as a large field-free region at the center of the trap and the ability to cool the entire apparatus,[12] make it a favorable platform for the integration of targets[13] and detectors[6] to study processes occurring in ionic systems. Here, we report the adaptation of an existing photoelectron-photofragment coincidence (PPC) spectrometer to include a cryogenically-cooled EIBT, allowing dissociative photodetachment (DPD) experiments to be performed on cold molecular anions and enhancing the ability to energetically resolve the dissociation dynamics of neutral molecular reaction intermediates and clusters.[14,15]

The use of translationally and internally cold neutral molecular beams has, over the last few decades, become a standard element of many gas-phase experiments. Supersonic jet expansions have been shown to produce molecules with vibrational temperatures below 100 K and rotational temperatures below 20 K, enabling extremely high-resolution spectroscopy to be carried out in the gas phase on a wide variety of cold molecular and cluster systems.[16] However, in the case of molecular ion beams the ionization process can reintroduce significant amounts of internal energy, particularly into vibrational degrees of freedom. For molecular ions that are efficiently created only late in the expansion or through multistep ion chemistry, some internal degrees of freedom remain excited, giving rise to characteristic "hot bands" in spectra. Significant internal excitation in anion precursors complicates analysis of photoelectron and photofragment kinetic energy spectra. Examples from this laboratory include studies of the acetyloxyl radical,[17] which was found to have up to 0.2 eV of extra internal energy residing in the precursor anion,[18] and the HOCO radical,[19] which was shown using the instrument described here to have contained as much as 0.6 eV of internal excitation in the HOCO anion.[14] Though this would seem to be an extreme amount of internal excitation, in small molecules the formation and vibrational energy redistribution mechanisms can be highly non-statistical, leading to large disparities between energy partitioning among internal degrees of freedom[20] and the inapplicability of the concept of temperature and thermal equilibrium among the degrees of freedom of a single molecule. Thus, in discussions here the term cooling should be interpreted loosely as the process of removing energy from the molecule.

Several approaches have been employed to reduce the effects of internal excitation. Cold ions can be generated by argon or hydrogen solvation in which the weakly-bound solvent is clustered with ions prior to mass selection.[21,22] Evaporation of the solvent removes heat from the ion, setting an upper limit to the internal energy (temperature) of the ion.[23] The solvent has been shown to exert a small influence on the spectroscopy of the ion in most cases, allowing for high-resolution measurements. Nanodroplet spectroscopy, a similar technique in which molecules are cooled by insertion into a large cluster of atoms, typically helium, has also shown the ability to produce high-resolution spectra of cold neutral molecules and ions.[24–27] Another technique employs a radiofrequency ion trap to store ions in a cryogenic environment surrounded by a cold buffer gas prior to measurement.[28,29] In these conditions thermalization of ions with the buffer gas removes internal

excitation from the ions over a period of several tens or hundreds of milliseconds. Once cold, experiments are either conducted inside the trap, or the ions may be extracted for further measurements.[30,31]

Unfortunately, these techniques are not suited for the PPC experiments performed in this laboratory.[32] PPC spectroscopy is a kinematically complete experiment in which dissociative neutral intermediates of known internal energy are created by photodetachment of an electron from a stable molecular anion. By collecting all resultant neutral fragments from the dissociation event in coincidence with the detached electron using time- and position-sensitive detectors, the correlated momenta and energies of all products can be calculated. This technique provides insight into the electronic structure of the parent anion and neutral species as well as the energy-resolved dynamics on the neutral potential energy surface. Coincidence experiments generally require a high duty cycle and low event rate to avoid contamination of data due to false coincidences, and thus low-repetition-rate techniques such as nanodroplets and radiofrequency ion traps may necessitate significantly longer acquisition times or increased difficulty in separating false coincidence events than current methods. Further, the addition of an extra body in Ar-tagging methods requires increased complexity in data analysis for multiparticle three-dimensional fragment imaging techniques and a reduction in overall detection efficiency per event due to the efficiency of microchannel plates. Finally, none of these techniques allow PPC experiments to be performed on ions as they cool and thus information related to the cooling process itself is lost.

In order to address these issues we have adapted an EIBT for use in PPC experiments. This trap is a type of focusing linear double-reflectron setup analogous to an optical resonator. Under ultrahigh vacuum conditions, this trap is capable of storing ion beams for many seconds. The EIBT is ideal because it can maintain ions in collimated, beam-like trajectories required for translational spectroscopy experiments and features a large field-free region in the center of the trap that can be used for electron detection. These features allow experiments to be performed on ions while they are trapped, providing the high (kHz) duty cycle required for coincidence experiments without the need to repeatedly cool ions on the hundred microsecond timescale. Furthermore, this type of trap is compact and relatively simple to construct and operate, making integration with the current experiment straightforward.

This EIBT has also been constructed to enable the mirror elements and surrounding blackbody radiation shields to be cooled to cryogenic temperatures, ensuring that trapped ions have minimal exposure to room temperature radiation. Under these conditions the stored ions can radiatively decay to ground or near ground vibrational and rotational levels on millisecond to second time scales. Additionally, the use of an intense, low-repetition-rate supersonic source allows inherently colder ions to be generated and injected into the trap. This allows study of the DPD of precursor anions with well-characterized internal energy distributions, giving increased energetic accuracy and opens new avenues of investigation that were not practical in a single-shot PPC instrument, such as the cooling processes of ions with long-lived ro-vibrational states and controlled internal excitation of anions prior to photodetachment.

II. EXPERIMENTAL

The cryo-PPC spectrometer consists of the same ion source and time-of-flight mass spectrometer previously reported[33] with virtually no modifications, and is depicted in Figure 1. Anions are synthesized in a 10 Hz pulsed supersonic expansion with a coaxial pulsed discharge crossed by a 1 keV electron beam, which can subsequently be intersected by a second pulsed supersonic beam if needed. This expansion is skimmed, accelerated to 4–12 keV, and rereferenced to ground in a fast potential switch. Anion packets typically 2–5 μs in length are separated by time of flight and guided into an electrostatic chopper ("mass gate") consisting of two parallel electrodes biased at $\pm$450 V to deflect ions into a microchannel plate (MCP) based timing detector, and pulsed to ground to allow the mass of interest to pass into the trap. The entrance mirror and lens are held at ground until the ion packet is fully in the trap cavity, and are then quickly switched to operational potential using fast high voltage switches. Ions with proper trajectories are stored in the trap and are lost primarily due to collisions with background gas. Trapped ions are bunched and phase-locked to a mode-locked kHz laser using a small RF potential on a coaxial cylindrical electrode, and ion bunch evolution is monitored using a charge-sensitive preamplifier (Amptek A250) attached to another coaxial electrode.[1,34] Photodetached electrons are detected intracavity, while resulting neutrals are collected downstream from the trap. Data from each detector is collected in coincidence, along with a timestamp for the amount of time trapped, using a CAMAC-based data acquisition system connected to a personal computer.

A. Trap design

The overall design of the ion trap assembly is shown in Figure 2, with a detailed view of the interaction region and electron detector in Figure 3. The plate thickness, spacing, and hole diameters of the individual electrodes in the mirror assemblies are identical to those previously described by the Zajfman group.[2] These mirror assemblies consist of a stack of reflecting electrodes coupled to a cylindrical electrostatic lens, with grounded electrodes at the front and rear of each assembly. Electrode spacing is set using insulating sapphire balls to enhance thermal conductivity. Each assembly is individually mounted to a vacuum flange via a thermally insulating system analogous to an optical kinematic mount, with a ball-bearing pivot and two linear manipulators at opposite corners to allow inclination about two axes. This design permits precise control of mirror alignment while the trap is under vacuum, alleviating the need to carefully control thermal contraction during temperature cycling. The angular resolution of this system is < 0.3 mrad. The total length of the trap cavity is 50 cm measured from the back of the first ground plate on the entrance mirror to the same plate on the exit mirror.

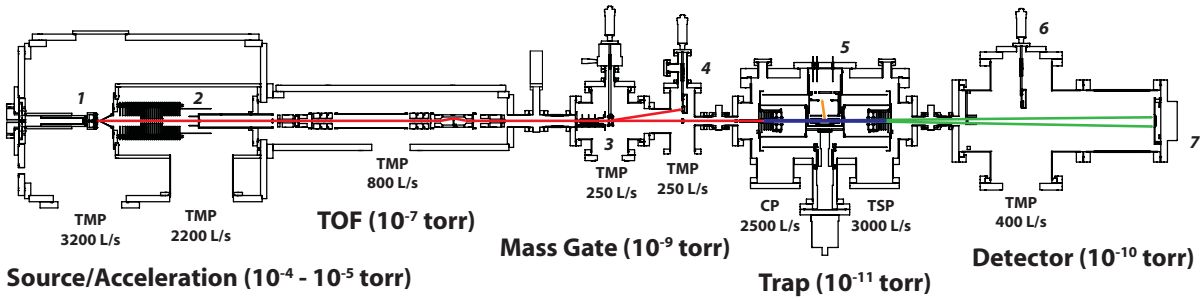

FIG. 1. (Color online) Overview of the cryo-PPC instrument. Labeled components are as follows: (1). Pulsed valve/discharge assembly. (2). Acceleration stack and potential switch. (3). Electrostatic chopper. (4). Pre-trap ion detector. (5). Electron detector. (6). Post-trap ion detector. (7). Neutral particle detector.

Two sets of radiation shields surround the trap cavity and are mounted directly on a closed-cycle He refrigerator (Austin Scientific, CryoPlex 1020). The inner set, held at ∼20 K, consists of cylindrical surfaces attached to a copper platform directly connected to the 2nd stage of the cryocooler. These cylindrical surfaces are attached to the rear grounded electrodes of the trap mirrors by several layers of flexible copper foil to provide good thermal contact throughout the 20 K region. Surrounding this assembly is a second set of polished copper shields attached to the 1st stage of the cryocooler and typically held at ∼50 K. These shields are also connected via stacked copper foils to a set of copper endcaps attached to the mirror assemblies, to reduce the heat load on the cold mirrors and eliminate line-of-sight from the room-temperature vacuum chamber to 20 K elements.

Trapping voltages are transferred to the mirrors by 0.8 mm diameter bare stainless steel wires to reduce thermal conductivity from the room-temperature feedthrus. The voltage on the trap lenses is provided by a high voltage power supply (Bertan 210B) attached directly to the exit side lens and through a fast push-pull high voltage switch (Behlke HTS series) on the entrance side lens to allow grounding during ion injection. Mirror voltages are generated by voltage division of the output of another high voltage power supply (Matsusada AE series) in a V, V/2, V/4, V/8 arrangement, again acting directly upon the exit mirror and through another fast HV switch on the entrance mirror. The slow RC time constant of the lower voltage electrodes is bypassed by the innate capacitance of the mirror plates and wiring, and tuning of the capacitance of the voltage divider allows all plates to be switched to full stable voltages with minimal drift well before the first recurrence of the ion packet in the trap.

B. Vacuum system

Since trapping lifetimes are inversely proportional to background pressure in this type of trap, pressures below 10^{-10} torr are essential to allow trapping for several seconds.[2] The trap assembly is housed within a custom-built 603 mm ID wire-seal vacuum chamber pumped by a 2500 L/s cryopump (Austin Scientific CP-8) and a home-built 3000 L/s titanium sublimation pump. Additional pumping occurs, when the entire assembly is cooled, by cryosorption of gases onto the system itself. Pressures are monitored using a UHV ion gauge (Varian) with an x-ray background of 6×10^{-12} torr, and base pressures of 2×10^{-11} torr are achieved after several days under vacuum.

The ion beam apparatus is constructed with several stages of differential pumping ensuring a low gas load from upstream sections by use of a 3 mm aperture between the mass gate and trap regions. A much larger 12 mm aperture must be used to separate the neutral detector chamber from the trap chamber in order to expose the full field of view of the

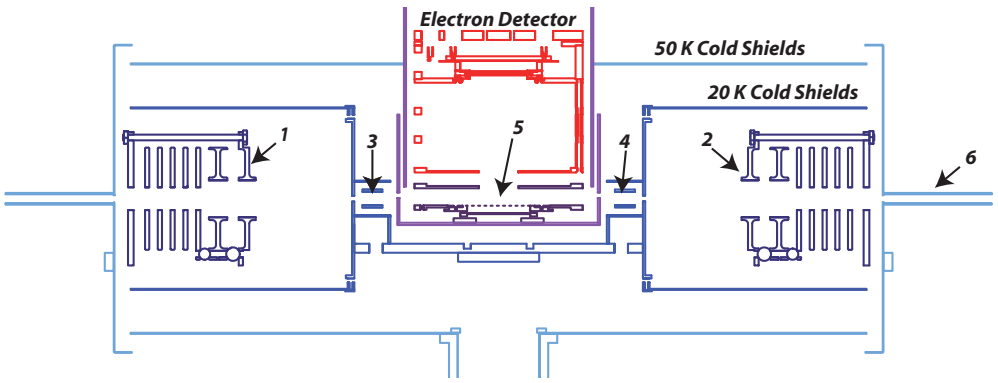

FIG. 2. (Color online) Detailed diagram of the trap assembly. Labeled components are as follows: (1). Entrance mirror. (2). Exit mirror. (3). Bunching electrode. (4). Pickup electrode. (5). Laser-ion interaction point. (6). Coaxial blackbody radiation baffles. Elements in dark blue are nominally 20 K, elements in light blue are nominally 50 K, and red is nominally room temperature. The magnetic shields span the 20–50 K range, and are shown in purple. Mirror electrode voltages are ordered in the same manner described in Ref. 2.

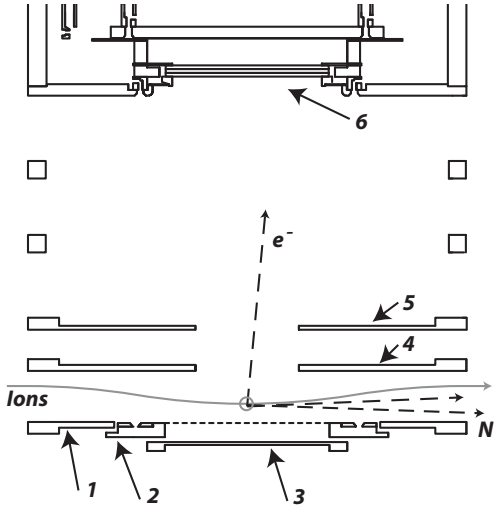

FIG. 3. Detail of the interaction region and electron detector. The interaction point is shown with a gray circle, and example electron (e^-) and neutral fragment (N) trajectories are shown. Labeled components are as follows: (1). Ion correction plate (positive bias). (2). Repeller plate and central grid (negative bias). (3). Electron background reducer plate (positive bias). (4). Extraction lens (grounded). (5). Focusing lens (positive bias). (6). Microchannel plates for electron detector. All parts have cylindrical symmetry. The ion trajectory through this region is exaggerated for clarity.

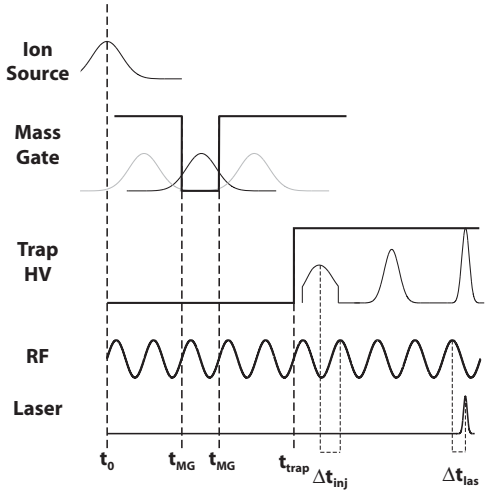

FIG. 4. Timing diagram showing the propagation of an ion pulse through the instrument and the relevant pulse times (long dashed lines), where t_0 is the time at which the beam potential is switched, t_{MG} is the mass gate opening and closing, and t_{trap} is the trap closing. The phases important to proper synchronization, the RF-injection phase (Δt_{inj}) and RF-laser phase (Δt_{las}), are denoted with short dashed lines. The rate of ion bunch evolution is greatly exaggerated.

multiparticle detector to the recoiling neutral particles, requiring lower pressures in the detector chamber. Experimental loads from these chambers typically raises the background pressure in the trap chamber by 1–2 $\times$ 10^{-11} torr.

C. Synchronization with pulsed laser

In order to ensure high ion density and good temporal overlap of oscillating ion pulses with the intersecting laser pulses, a stable bunching and synchronization scheme is required, with timings shown diagrammatically in Figure 4. Application of a small RF field on a cylindrical electrode along the oscillation axis at the fundamental (typically ~100 kHz), or a harmonic, of the natural ion oscillation frequency can force the ions to bunch in packets <200 ns long. Ion oscillation frequencies must be near-resonant with this signal to optimize this effect. This can be achieved by tuning the beam energy on the order of 0.1%. The synchronization system also eliminates detachment signal from anions travelling in the reverse direction in the trap, increasing the coincidence rate of the experiment and removing a significant Doppler offset in photoelectron images as seen in Figure 5. Triggerable kHz q-switched lasers can be simply used by prescaling the RF frequency to an appropriate value for use as the laser repetition rate. However, the use of femtosecond or picosecond modelocked lasers is more complex due to the constraint that the laser repetition rate must be fixed to a divisor of the laser master oscillator frequency and thus is only coarsely adjustable.

Consistent phase locking of the bunching RF field to the pulsed laser is maintained by synchronizing the bunching signal with the master oscillator of the laser. The system implemented for this purpose, outlined in Figure 6, begins with integer division and multiplication of the laser master oscillator frequency, generating a phase-locked signal that can be used to override the reference oscillator of an analog function generator (HP 3325B). This forces the function generator output to be phase-locked to the laser repetition rate and allows simple control over the laser-RF phase and the RF amplitude through normal function generator operation. The current laser systems used are a Ti-Sapphire regenerative amplifier (Clark-MXR, CPA2000) seeded by a 43.58 MHz diode-pumped Kerr-lens-modelocked fiber oscillator, and an actively modelocked, q-switched, cavity dumped Nd:YAG (Quantronix 116) with a cavity frequency of 50.01 MHz. The Ti:Sapphire system will be used as the example for the synchronization system, though the approach is essentially the

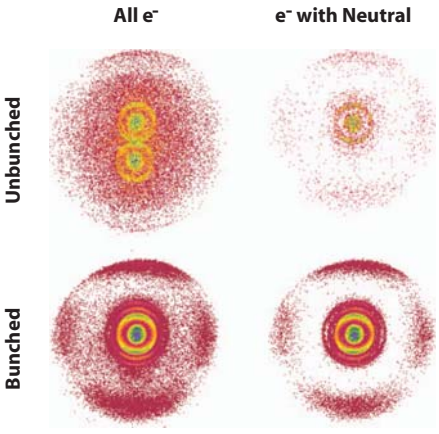

FIG. 5. (Color online) Example of unbunched and bunched photoelectron images for photodetachment of $DOCO^-$ at 775 nm. For each set of conditions, the images in the first column are of all electrons, regardless of neutral signal, while the second column images are from events with one neutral particle detected in coincidence. In these images, a signal present at large radii arising from two-photon absorption by a single ion is intentionally cut by the edge of the detector, allowing enhanced resolution for low-energy electrons.

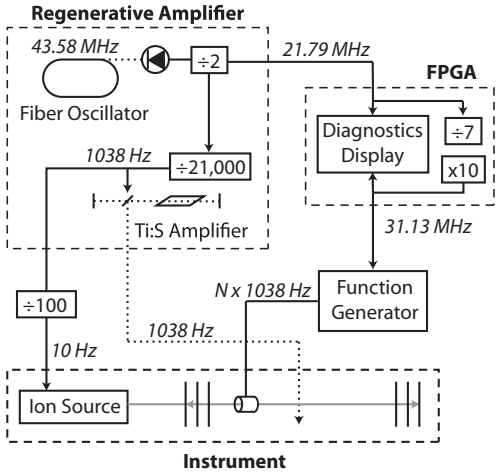

FIG. 6. Diagram of the phaselocking system. Solid connectors represent electrical signals and dotted connectors represent laser light.

same for either laser. The fiber oscillation rate is prescaled by 42 000 to drive the regenerative amplifier system, leading to a repetition rate of 1038 Hz. By multiplying the fiber oscillator frequency by 5/7, a phase-locked 31.13 MHz signal is obtained which drives the nominally 30.00 MHz reference oscillator of the function generator, with a factor of 1.038 (by definition exactly the laser rate divided by 1000) relating the two. Thus any frequency input to the function generator that is an integer multiple of 1000 will automatically induce bunching at an integer multiple of the laser repetition rate. In this case, the "frequency" entered into the function generator is actually the number of RF periods per laser shot $\times 1000$, which when scaled by 1.038 gives the precise bunching frequency. The function generator reference frequency is synthesized in the phase-locked loop segments of a field-programmable gate array (Altera Cyclone II), which also provides diagnostic systems. This synchronization technique typically results in a $\sim$10 ns RMS jitter between the RF and laser pulse phases, with a phase resolution of 0.03% of the RF period. Bunching at the second harmonic of the ion oscillation frequency has been found to produce temporally shorter ion bunches with negligible impact on the laboratory frame energy distribution of trapped ions (see Sec. III C).

D. Intracavity electron detector

The field-free nature of the center of this type of trap allows relatively simple integration of a velocity-map imaging (VMI) (Ref. 35) photoelectron detector in the trap cavity. Electrons are extracted perpendicularly to the laser-ion plane, with electric fields in the interaction region typically $\sim$10 V/cm. Deflection of the ion beam by the extraction field requires correction of the ion trajectories in order to maintain stable trapping. This is accomplished by splitting the repeller in standard VMI designs into two concentric discs, a repeller and corrector, with opposite polarities. As ions traverse this region, they are first deflected downward by the first correction field, then deflected upward by the repeller and leveled by the second correction field. Proper adjustment of voltage of the correction plate allows undetached ions to exit the electron detector on the same trajectory they entered, while still providing a homogeneous repeller field to extract electrons to the detector, and ensuring the neutral center-of-mass recoil trajectory remains parallel to the ion beam. Vertical deflections of $\sim$0.5 mm are calculated for typical ion masses and beam energies. Additionally, the central area of the repeller is composed of a 90% transmissive grid with a positively biased plate underneath, a design that has been shown to significantly reduce electron background from scattering of photons in ultraviolet experiments.[36]

The VMI extraction optics are held at $\sim$20 K, and the entire photoelectron spectrometer is encased in a magnetic shield composed of Cryoperm-10 on the cold side and mu-metal on the warm side (Amuneal, Inc.). Since the detectors used in these experiments are time- and position-sensitive, the VMI geometry has been optimized to increase the dynamic range for the electron time of arrival, enhancing timing resolution. The detector is composed of a Z-stack of microchannel plates (MCPs) whose emitted charge is detected by a wedge-and-strip anode[37] to determine position of arrival, and capacitively coupled to a fast amplifier feeding a constant fraction discriminator and time-to-amplitude converter for timing measurement, as previously described.[33]

E. Experimental details

All timing signals for source, mass gate, and trap triggers are controlled by a digital delay generator (Stanford Research DG645) triggered by and prescaled to 1/100th of the laser repetition rate ($\sim$10 Hz) to achieve consistent timing between ions, RF bunching, and laser pulses. The ion beam energy must be tuned to produce a natural oscillation frequency close to the bunching frequency, with example oscillation frequencies for a number of ions shown in Table I. Optimization of the synchronization system involves two phases with respect to the RF signal: (1) the phase at which ions are injected, controlled by the digital delay generator, and (2) the phase at which the laser pulse crosses the ion beam, controlled by the function generator. Laser pulses are injected perpendicular to the trap axis in the center of the trap, and focused to a diameter of less than 1 mm. Neutral particles resulting from photodetachment recoil over a 1.29 m flight path along the trap centerline with a center-of-mass velocity equal

TABLE I. Selected ion oscillation frequencies for given trapping voltages and beam energies.

			Voltages (V)		
Anion	Mass (amu)	Freq. (kHz)	Beam	Mirror	Lens
O^-	16	259.50	6874	10 500	6360
O_2^-	32	184.70	7034	10 580	6524
$HOCO^-$	45	154.45	6903	10 550	6467
$DOCO^-$	46	152.55	6820	10 550	6294
NO_2^-	46	153.63	6937	10 550	6421
O_4^-	64	130.14	6996	10 550	6468
$C_4H_9O^-$	73	121.50	6875	10 550	6337

to the beam velocity and are detected by another 40 mm MCP based time- and position- sensitive quad-delay-line multiparticle detector.[33] Data is acquired on an event-by-event basis in a similar system to that described previously. In order to group events by trapping time, each laser pulse increments a CAMAC counter, which is reset for each trap injection. Recording this count for each event allows for trap time gating of data during analysis and also allows dynamics to be monitored as a function of trapping time.

III. RESULTS

A. Trapping lifetimes

No detailed study of trapping lifetimes has been performed on this instrument; however, approximate lifetimes can be extracted directly from PPC data by binning photoelectrons as a function of trapping time. Several example systems are shown in Figure 7, revealing exponential lifetimes on the order of seconds at pressures in the high 10^{-11} torr range. Since the data used for lifetime extraction is taken from bunched experiments, the first 500 ms are ignored in exponential fits, removing the influence of the initial adjustment of the ion packet to the bunching field and any other short-time dynamical effects. After this time, decay is essentially monoexponential with no significant difference in decay rates seen between bunched and unbunched operation. Unsurprisingly, larger systems such as the tert-butoxide anion show shorter lifetimes despite their reduced path length per unit trapping time, likely due to larger charge-exchange and collisional detachment cross-sections with the background gas,[38] though a detailed analysis of these loss mechanisms is beyond the scope of this work. While experiments are typically performed over 1–5 s trapping time, significant signal remains at the end of the trap cycle allowing experiments over much longer times to be performed if necessary.

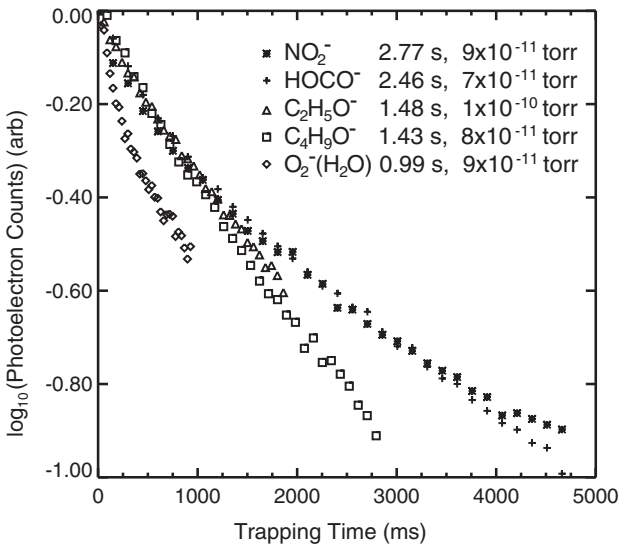

FIG. 7. Decay times for various species and operational pressures. The vertical axis represents the number of photoelectrons detected in a given trapping interval in logarithmic scale. Fast dynamics due to bunching effects on the overall photodetachment effects are seen for the first few hundred milliseconds, and decay times are measured after the first 500 ms of trapping to reduce the influence of this effect. All data is taken at ~7 keV beam energy except $C_2H_5O^-$ which is 4 keV.

B. Recoil trajectories

A crucial requirement for these translational spectroscopy measurements is the attainment of a low-divergence ion beam with a small cross-section at the interaction region, yielding a small distribution of center-of-mass positions at the neutral particle detector. Optimization of this distribution was performed by observing the distribution of neutral particle impacts on the neutral particle detector for non-dissociative photodetachment of NO_2^- at 388 nm. Representative results of this optimization are shown in Figure 8. A strong correlation exists between observed signal rate and neutral position distribution, implying that a narrow, well-collimated beam is only reliably obtained through reduction of the stable trapping phase space. The minimum practical neutral distribution, as projected onto the neutral detector, was ~0.9 mm standard deviation with a circular and approximately Gaussian profile. This is significantly smaller than the 3 mm injected beam diameter as determined by the entrance apertures upstream from the trap and approximately the same size as the laser focus. At the lower limit of this optimization, fragment times-of-flight were found to be broadened to later times, implying that trapped ion laboratory energies are not conserved and that inelastic ion-ion scattering or scattering off of background gas may become significant under these conditions. This is consistent with a small stable phase space necessarily leading to a narrow beam, with ions scattered to higher energy being lost while ions scattered to lower energy remain in the stable trapping space. However, it is not clear at this time what the mechanism underlying this effect is. No ion heating was observed within the experimental photoelectron resolution in this mode of operation implying these ion-ion collisions do

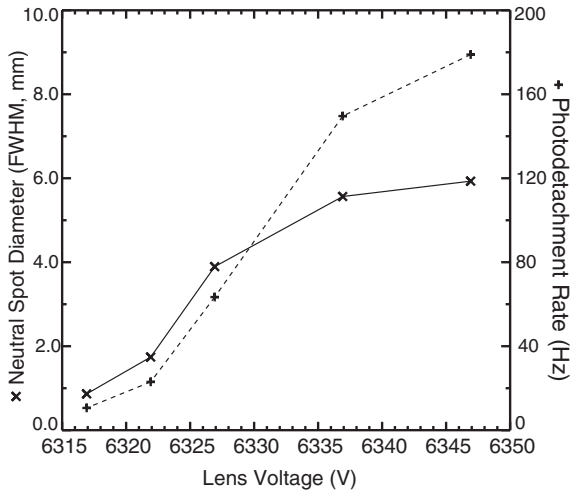

FIG. 8. Neutral position distribution width (FWHM) (×) and photodetachment rate (+) as a function of trap lens voltage. Here the beam energy and mirror voltages are 6872 eV and 10.490 kV respectively, and ions are not bunched. Total trapping time is 90 ms.

not partition significant amounts of energy into internal degrees of freedom.

C. Bunching properties

Ion packet dispersion was found to occur on timescales of several tens of milliseconds, requiring the use of bunching even for short trapping times. However, the effect of bunching on the overall kinetic energy spread of the ions must be minimal in order for the three-dimensional neutral particle imaging scheme to be effective. This can be directly determined by observing the time-of-flight of stable neutrals, again from NO_2^- photodetachment, in which the spread of times-of-flight of the neutral particle can be interpreted as an energy spread. In order to assess the effect of the bunching signal amplitude on the beam energy distribution, fragment flight times were recorded at different RF amplitudes, as shown in Figure 9. The onset of stable bunching is ~0.6 $V_{p\text{-}p}$, and the kinetic energy spread remains constant up to 1 V. In this range bunching appears to have little overall effect on the ion velocity profile, and the bunching field acts instead as a time-dependent delay ($\pm \Delta t$) rather than increasing or decreasing the kinetic energies of ions in different parts of the ion packet. This is supported by the fact that no observable change in transverse velocity distributions is seen under low bunching voltages.

A strong dependence on the injection-RF phase was found in the beam energy spread, shown in Figure 10 at 1 $V_{p\text{-}p}$ amplitude. It is clear that injection off of the optimal phase splits the ion packet into two, each with slightly different average lab frame energies. This effect is less apparent at 0.6 $V_{p\text{-}p}$ amplitude. This effect implies that the "adiabaticity" of the bunching effect only holds when ions are injected near the correct phase, allowing the bunching field to serve only to compress and maintain bunch width throughout the trapping cycle.

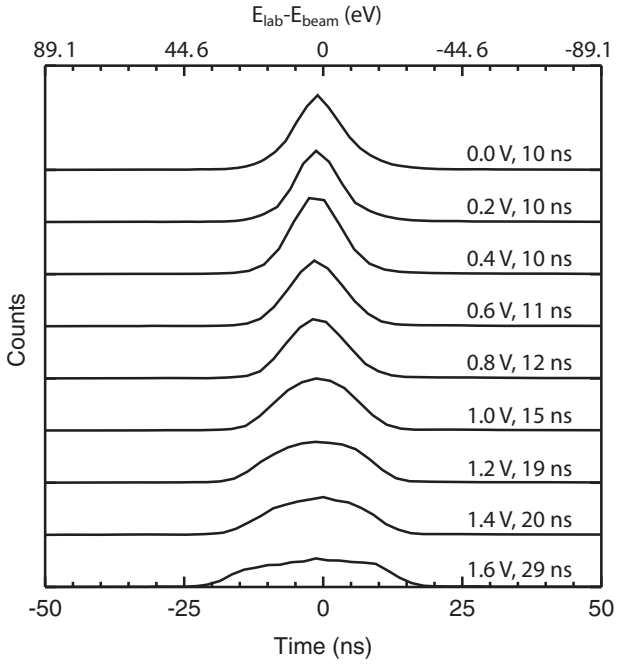

FIG. 9. Bunch velocity distribution vs. RF amplitude for NO_2^- photodetachment at 388 nm and 6930 eV beam energy. Bunching phases are optimized at 1.0 $V_{p\text{-}p}$, and the bunching frequency is the second harmonic of the natural ion oscillation frequency of 153.65 kHz. The total trapping time is 90 ms. For each trace, the bunching voltage and peak FWHM are listed.

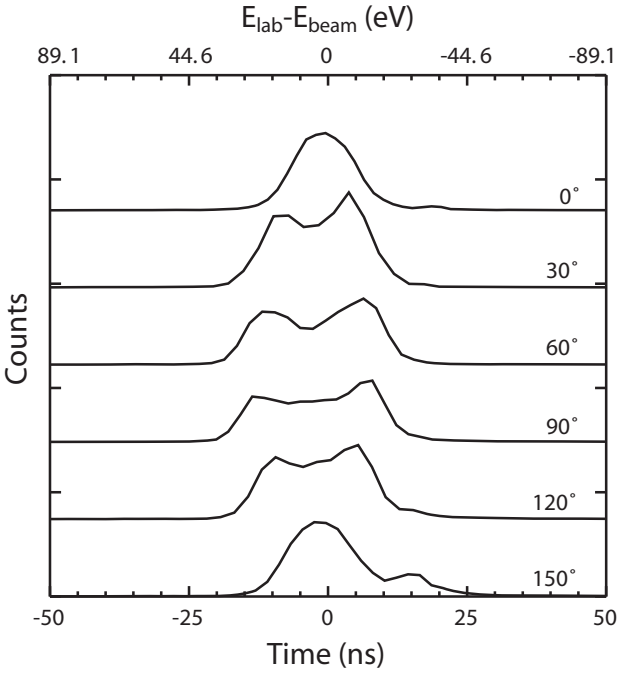

FIG. 10. Bunch energy distribution vs. RF-injection phase shift for the same conditions as Figure 9. Phases given are with respect to the optimal injection phase. In this case the bunching amplitude is fixed at 1 $V_{p\text{-}p}$.

D. Cooling

An unexpected result that has generally been found with this instrument is that ions in the trap are almost entirely cold throughout the trapping cycle. This is likely due to the ability to generate colder ions in the strong 10 Hz supersonic expansion than the weaker 1 kHz expansion used in previous single-shot experiments in this laboratory.[19] It is also difficult to observe cooling on timeframes shorter than a few milliseconds, due to the 1 kHz laser repetition rate and the fact that ions are trapped approximately 800 μs prior to the first laser pulse, leading to cooling on these timescales to be missed. However, it has been possible to alter the ion source conditions to form internally excited anions and observe long-time cooling. One example is given in Figure 11 for generation of the HOCO radical anion in "hot" source conditions. A clear evolution of the spectrum from early to late trapping times can be seen, as peaks corresponding to the OCO bending vibration of HOCO gradually sharpen towards the end of the trapping period. Though hot anions have thus far proven difficult to generate in the 10 Hz source, it is expected that larger systems and clusters will more readily be generated with measurable amounts of internal energy, allowing radiative cooling dynamics to be observed on long timescales.

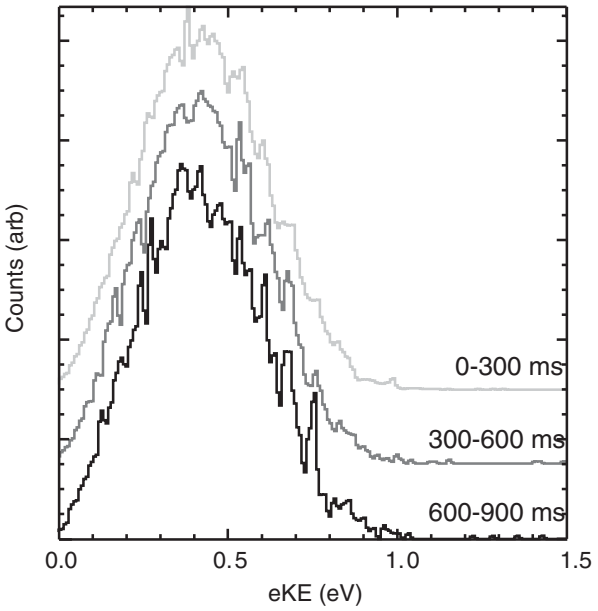

FIG. 11. An example of cooling in $HOCO^-$ anions. All data is from a single data file and each spectrum is composed of events falling within the specified trapping time window. Significant sharpening of spectral features is apparent at later times.

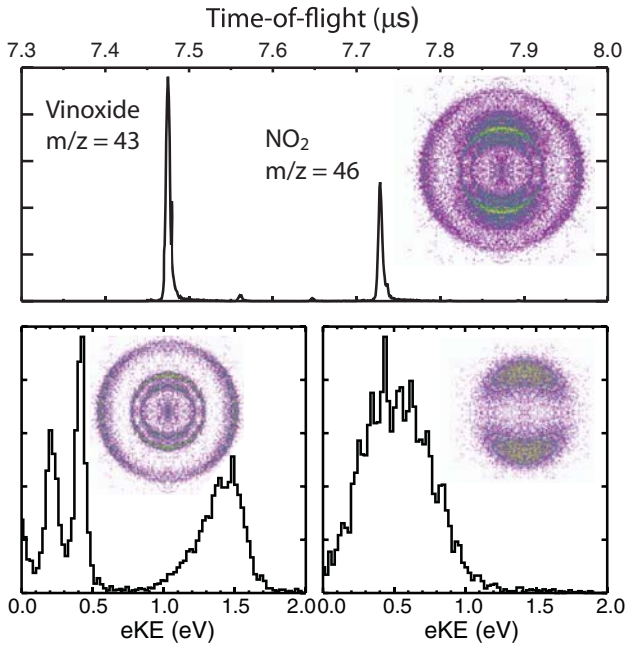

FIG. 12. (Color online) An example of multimass operation. The top panel depicts the times-of-flight of the neutral fragments following photodetachment, with the photoelectron image recorded at a photon energy of 3.20 eV for electrons coincident with any neutral particle inset. The bottom left panel is the electron kinetic energy spectrum extracted by enforcing coincidence with only neutrals of m/z = 43, ($C_2H_3O^-$) with the resulting photoelectron image inset. The bottom right panel shows the same results for m/z = 46 (NO_2^-). All images are quadrant-symmetrized for clarity.

E. Multimass experiments

An additional benefit of operating the PPC spectrometer with the ion trap is the ability to collect photoelectron spectra of several species of differing mass simultaneously, particularly when bunching is not enabled. Since all ions traveling within the trap cavity when the entrance mirror closes will be trapped, the coincidence detection scheme allows for electrons from all species to be recorded simultaneously and later separated by mass. This is accomplished by gating, in post-experimental analysis, on electrons in coincidence with specific range of neutral particle time-of-flight corresponding to a given species. This "high-throughput photoelectron spectroscopy" mode has led, for example, to the extraction of $NO^-(CD_4)$ and $NO^-(H_2O)$ spectra[39] from an experiment performed on the $DOCO^-$ anion. An example of this extraction is outlined in Figure 12, with photoelectron images and spectra extracted from peaks in the fragment TOF spectrum corresponding to the vinoxide ($C_2H_3O^-$) anion[40] and NO_2^-, both of which are trapped simultaneously. No detectable crosstalk between the spectra of the two species is seen, allowing photoelectron spectra of multiple species to be collected in a survey experiment.

IV. SUMMARY

The cryo-PPC spectrometer has proven to generate better-resolved data at higher acquisition rates than the single-shot instrument with only a nominal increase in difficulty of operation. In addition, new opportunities are now available for extension of the PPC technique to study systems that were not previously possible due to the ability to couple low-repetition-rate sources, such as laser ablation or electrospray ionization, to the kHz rates required for coincidence experiments. New opportunities also exist for studying vibrationally or isomerically prepared systems by laser excitation in the ion source, allowing for much greater control over the conditions and identities of species studied.

ACKNOWLEDGMENTS

The authors gratefully acknowledge the Zajfman group at the Weizmann institute, particularly M. L. Rappaport, for advice and plans for the trap electrodes. C. R. Vane, M. R. Fogle, and R. D. Thomas provided helpful discussions. Development of the synchronization system was aided by A. White and G. Kassabian of the UCSD Physics Electronics Shop. This work was supported by the U. S. Department of Energy under (DOE) Grant Number DE-FG03-98ER14879.

[1]W. H. Benner, Anal. Chem. **69**, 4162 (1997).
[2]M. Dahan, R. Fishman, O. Heber, M. Rappaport, N. Altstein, D. Zajfman, and W. J. Van Der Zande, Rev. Sci. Instrum. **69**, 76 (1998).
[3]Y. Toker, O. Aviv, M. Eritt, M. L. Rappaport, O. Heber, D. Schwalm, and D. Zajfman, Phys. Rev. A **76**, 53201 (2007).
[4]L. Knoll, K. G. Bhushan, N. Altstein, D. Zajfman, O. Heber, and M. L. Rappaport, Phys. Rev. A **60**, 1710 (1999).
[5]P. Reinhed, A. Orbán, J. Werner, S. Rosén, R. D. Thomas, I. Kashperka, H. A. B. Johansson, D. Misra, L. Brännholm, M. Björkhage, H. Cederquist, and H. T. Schmidt, Phys. Rev. Lett. **103**, 213002 (2009).
[6]O. Aviv, Y. Toker, M. Errit, K. G. Bhushan, H. B. Pedersen, M. L. Rappaport, O. Heber, D. Schwalm, and D. Zajfman, Rev. Sci. Instrum. **79**, 83110 (2008).
[7]H. Pedersen, S. Altevogt, B. Jordon-Thaden, O. Heber, L. Lammich,

M. Rappaport, D. Schwalm, J. Ullrich, D. Zajfman, R. Treusch, N. Guerassimova, M. Martins, and A. Wolf, Phys. Rev. A **80**, (2009).
[8]K. G. Bhushan, S. C. Gadkari, J. V. Yakhmi, and V. C. Sahni, Rev. Sci. Instrum. **78**, 83302 (2007).
[9]J. B. Greenwood, O. Kelly, C. R. Calvert, M. J. Duffy, R. B. King, L. Belshaw, L. Graham, J. D. Alexander, I. D. Williams, W. A. Bryan, I. C. E. Turcu, C. M. Cacho, and E. Springate, Rev. Sci. Instrum. **82**, 43103 (2011).
[10]D. Zajfman, Y. Rudich, I. Sagi, D. Strasser, D. W. Savin, S. Goldberg, M. Rappaport, and O. Heber, Int. J. Mass Spectrom. **229**, 55 (2003).
[11]L. H. Andersen, O. Heber, and D. Zajfman, J. Phys. B **37**, R57 (2004).
[12]M. Lange, M. Froese, S. Menk, J. Varju, R. Bastert, K. Blaum, J. R. C. Lopez-urrutia, F. Fellenberger, M. Grieser, R. Von Hahn, O. Heber, K.-U. Kuehnel, F. Laux, D. A. Orlov, M. L. Rappaport, R. Repnow, C. D. Schroeter, D. Schwalm, A. Shornikov, T. Sieber, Y. Toker, J. Ullrich, A. Wolf, and D. Zajfman, Rev. Sci. Instrum. **81**, 55105 (2010).
[13]O. Heber, P. D. Witte, A. Diner, K. G. Bhushan, D. Strasser, Y. Toker, M. L. Rappaport, I. Ben-itzhak, N. Altstein, D. Schwalm, A. Wolf, and D. Zajfman, Rev. Sci. Instrum. **76**, 13104 (2005).
[14]C. J. Johnson and R. E. Continetti, J. Phys. Chem. Lett. **1**, 1895 (2010).
[15]C. J. Johnson, B. L. J. Poad, B. B. Shen, and R. E. Continetti, J. Chem. Phys. **134**, 117106 (2011).
[16]R. E. Smalley, L. Wharton, and D. H. Levy, Acc. Chem. Res. **10**, 139 (1977).
[17]Z. Lu and R. E. Continetti, J. Phys. Chem. A **108**, 9962 (2004).
[18]X. B. Wang, H. K. Woo, L. S. Wang, B. Minofar, and P. Jungwirth, J. Phys. Chem. A **110**, 5047 (2006).
[19]Z. Lu, Q. Hu, J. E. Oakman, and R. E. Continetti, J. Chem. Phys. **126**, 194305 (2007).
[20]M. E. Sanz, M. C. Mccarthy, and P. Thaddeus, J. Chem. Phys. **122**, 194319 (2005).
[21]M. Okumura, L. I. Yeh, J. D. Myers, and Y. T. Lee, J. Phys. Chem. **94**, 3416 (1990).
[22]C. G. Bailey, J. Kim, C. E. H. Dessent, and M. A. Johnson, Chem. Phys. Lett. **269**, 122 (1997).
[23]S. B. Nielsen, P. Ayotte, J. A. Kelley, and M. A. Johnson, J. Chem. Phys. **111**, 9593 (1999).
[24]C. Callegari, K. K. Lehmann, R. Schmied, and G. Scoles, J. Chem. Phys. **115**, 10090 (2001).
[25]J. Kuepper and J. M. Merritt, Int. Rev. Phys. Chem. **26**, 249 (2007).
[26]G. N. Makarov, Phys. Usp. **47**, 217 (2004).
[27]J. P. Toennies and A. F. Vilesov, Ann. Rev. Phys. Chem. **49**, 1 (1998).
[28]D. Gerlich and S. Horning, Chem. Rev. **92**, 1509 (1992).
[29]X. B. Wang, H. K. Woo, and L. S. Wang, J. Chem. Phys. **123**, 51106 (2005).
[30]X.-B. Wang and L.-S. Wang, Rev. Sci. Instrum. **79**, 73108 (2008).
[31]M. Z. Kamrath, R. A. Relph, T. L. Guasco, C. M. Leavitt, and M. A. Johnson, Int. J. Mass Spectrom. **300**, 91 (2011).
[32]R. E. Continetti, Ann. Rev. Phys. Chem. **52**, 165 (2001).
[33]K. A. Hanold, A. K. Luong, T. G. Clements, and R. E. Continetti, Rev. Sci. Instrum. **70**, 2268 (1999).
[34]H. B. Pedersen, D. Strasser, B. Amarant, O. Heber, M. L. Rappaport, and D. Zajfman, Phys. Rev. A **65**, 42704 (2002).
[35]A. Eppink and D. H. Parker, Rev. Sci. Instrum. **68**, 3477 (1997).
[36]B. F. Parsons, S. M. Sheehan, K. E. Kautzman, T. A. Yen, and D. M. Neumark, J. Chem. Phys. **125**, 244301 (2006).
[37]C. Martin, P. Jelinsky, M. Lampton, R. F. Malina, and H. O. Anger, Rev. Sci. Instrum. **52**, 1067 (1981).
[38]H. B. Pedersen, D. Strasser, O. Heber, M. L. Rappaport, and D. Zajfman, Phys. Rev. A **65**, 42703 (2002).
[39]B. L. J. Poad, C. J. Johnson, and R. E. Continetti, Faraday Discuss. **150**, 481 (2011).
[40]M. S. Bowen and R. E. Continetti, J. Phys. Chem. A **108**, 7827 (2004).